

# Chapter 25

## Multifractal Characterization of Apple Pore and Ham Fat-Connective Tissue Size Distributions Using Image Analysis

Fernando Mendoza, Nektarios Valous, Adriana Delgado, and Da-Wen Sun

### 25.1 Application of Fractal and Multifractal Analysis to Biological Material

Fractal and multifractal concepts have been increasingly applied in various fields of science to describe the complexity and self-similarity of nature. A fractal describes a rough or fragmented geometric shape that can be subdivided into parts, each of which is at least approximately a reduced-size copy of the whole. Fractal dimensions offer a systematic approach to quantifying irregular patterns that contain an internal structure repeated over a range of scales (Mandelbrot 1992). Estimations of fractal dimension are based on the box-counting technique, which allows obtaining the scaling properties of 2-D fractal objects (e.g., from binary images) by covering the images with boxes size  $\varepsilon$  and counting the number of boxes containing at least one pixel representing the object or structure under study. However, the disadvantage of the box-counting technique is that the process does not consider the amount of mass inside a box and therefore is not able to resolve regions with high or low density of mass. Biological materials are frequently complex in the distribution of their components or structures, which could be of interest to characterize and to quantify, and therefore, simple fractal dimension estimations may not be enough to appropriately characterize these materials.

By contrast, multifractal methods are suitable for characterizing a complex spatial arrangement of mass because they can resolve local densities (Vicsek 1992). Multifractal formalisms involve decomposing self-similar measures into intertwined fractal sets, which are characterized by their singularity strength and fractal dimension. Multifractal characterization does not require a single dimension, but rather a sequence of generalized fractal dimensions. Thus, a combination of all the fractal sets produces a multifractal spectrum that can characterize variability and heterogeneity of the studied variables (Kravchenko et al. 1999). The advantage of

---

F. Mendoza (✉), N. Valous, A. Delgado, and D.-W. Sun  
FRCFT Group, Biosystems Engineering, UCD Agriculture & Food Science Centre, University College Dublin, Belfield D4, Ireland  
e-mail: fmendoza@ing.puc.cl; dawen.sun@ucd.ie

the multifractal approach is that multifractal parameters can be independent of the size of the studied objects (Cox and Wang 1993), and that no assumptions are required about the data following any specific distribution (Scheuring and Riedi 1994). This type of analysis has been successfully applied to plant science, ecology, and agronomy research for study of vegetation patterns (Scheuring and Riedi 1994), zooplankton biomass (Pascual et al. 1995), root systems of legumes (Ketipearachchi and Tatsumi 2000), spatial and temporal variability of residual soil  $\text{NO}_3\text{-N}$  and corn grain yield (Eghball et al. 2003), and soil structure under long-term wastewater irrigation (Xiaoyan et al. 2007), among others. However, very little further information exists about the multifractality in food samples at micro and macro levels and their related properties.

The objective of this chapter is to give an overview of the multifractal theory as applied to natural objects and systems, and to illustrate with two examples the complete application of this approach for characterizing contrasting PSD in apple tissue and FSD in cooked pork ham images. The identification of potential multifractal parameters useful for quality characterization and classification of these samples will be a final aim as well. PSD in apple tissue and FSD in pork hams are the fundamental physical properties analyzed in assessing their quality. In apple tissue, PSD is related to the mass-transport phenomena characteristics and complexity of  $\text{O}_2$  and  $\text{CO}_2$  diffusivity, and in the case of hams, FSD is related to the sensory properties such as texture, taste, quality of raw meat, and visual appearance. In both food products, accurate representation of these microstructural properties is needed for objective quality characterization and prediction during apple preservation and ham formulation.

## 25.2 Theory of MFA

Measurement of multifractals mainly involves measuring a statistical distribution, which in turn yields useful information even if the underlying structure does not show a self-similar or self-affine behavior (Plotnick et al. 1996). In a homogeneous system, the number  $N$  of features of a certain size  $\varepsilon$  varies (Chhabra and Jensen 1989; Everstz and Mandelbrot 1992; Vicsek 1992):

$$N(\varepsilon) \propto \varepsilon^{-D_0}, \quad (25.1)$$

where the fractal dimension  $D_0$ ,

$$D_0 = \lim_{\varepsilon \rightarrow 0} \frac{\log N(\varepsilon)}{\log \frac{1}{\varepsilon}} \quad (25.2)$$

can be measured by counting number  $N$  of boxes needed to cover the object under investigation for increasing box size  $\varepsilon$  and estimating the slope of a log-log plot

(i.e., using box-counting method). For heterogeneous or nonuniform systems, the probability within the  $i$ th region  $P_i$  scales as:

$$P_i(\varepsilon) = \varepsilon^{\alpha_i} \tag{25.3}$$

where  $\alpha_i$  is the Lipschitz-Hölder exponent characterizing density in the  $i$ th box (Halsey et al. 1986). One technique to determine multifractal parameters is to cover a measure with boxes size  $\varepsilon$ . The number of boxes  $N(\alpha)$  where the probability has values in the interval  $(\alpha, \alpha + d\alpha)$  is found to scale as (Halsey et al. 1986; Chhabra and Jensen 1989):

$$N(\alpha) \propto \varepsilon^{-f(\alpha)} \tag{25.4}$$

where  $f(\alpha)$  can be defined as the fractal dimension of the set of boxes with singularities  $\alpha$ . The exponent  $\alpha$  can take on values from the interval  $(\alpha_{-\infty}, \alpha_{+\infty})$ , and  $f(\alpha)$  is usually a single-humped function with a maximum at  $df(\alpha(q))/d\alpha(q) = 0$ , where  $q = 0$ ,  $f_{\max}$  is equal to the box-counting or  $D_0$  (Vicsek 1992; Gouyet 1996). In practice, using the box-counting method, for every box  $i$  the probability of a *containing object*, also called the partition function, is obtained for different moments  $q$ , which can vary from  $-\infty$  to  $+\infty$ . The partition function is represented by  $\mu(q, \varepsilon)$  and defined as (Chhabra and Jensen 1989):

$$\mu(q, \varepsilon) = \sum_{i=1}^{N(\varepsilon)} P_i^q(\varepsilon) \tag{25.5}$$

Multifractal sets can also be characterized on the basis of the generalized dimensions of the  $q$ th moment orders of a distribution,  $D_q$  (Hentchel and Procaccia 1983). Based on the work of Rényi (1995) they are defined as:

$$D_q = \lim_{\varepsilon \rightarrow 0} \frac{1}{1 - q} \frac{\log \sum_{i=1}^{n(\varepsilon)} P_i^q}{\log \varepsilon} \tag{25.6}$$

and when  $q = 1$ , things become tricky and can be computed as:

$$D_1 = \lim_{\varepsilon \rightarrow 0} \frac{\sum_{i=1}^{n(\varepsilon)} P_i \log P_i}{\log \varepsilon} \tag{25.7}$$

The generalized dimension  $D_q$  is a monotone decreasing function for all real  $q$  values within the interval  $(-\infty, +\infty)$ . When  $q < 0$ ,  $\mu$  emphasizes regions in the distribution with less concentration of a measure, whereas the opposite is true for  $q > 0$  (Chhabra and Jensen 1989). This means that the sum in the numerator of

(25.10) is dominated by the highest values of  $P_i$  for  $q > 0$ , and the lowest values of  $P_i$  for  $q < 0$ .

The partition function (a log-log plot of the quantity  $\mu(q, \varepsilon)$  over  $\varepsilon$  for different  $q$  yields) scales as:

$$\mu(q, \varepsilon) \propto \varepsilon^{-\tau(q)} \quad (25.8a)$$

or

$$\tau_q = \lim_{\varepsilon \rightarrow 0} \frac{\log \mu(q, \varepsilon)}{\log \frac{1}{\varepsilon}} \quad (25.8b)$$

where  $\tau(q)$  is the mass or correlation exponent of the  $q$ th order defined as (Halsey et al. 1986):

$$\tau(q) = (q - 1)D_q \quad (25.9)$$

The connection between the power exponents  $f(\alpha)$  (25.4) and  $\tau(q)$  (25.6) is made via the Legendre transformation (Callen 1985; Halsey et al. 1986; Chhabra and Jensen 1989):

$$f(\alpha(q)) = q\alpha(q) - \tau(q) \quad (25.10)$$

and

$$\alpha(q) = \frac{d\tau(q)}{dq} \quad (25.11)$$

The  $f(\alpha)$  spectrum and the generalized dimensions contain the same information, both characterizing an interwoven ensemble of fractal dimensions  $f(\alpha_i)$ . In each of the  $i$ th fractals, the observable  $P_i$  scales with the Lipschitz-Hölder-exponent  $\alpha_i$ .

The generalized dimensions for  $q = 0, 1$ , and  $2$  mathematically describe the defined fractal dimensions known as  $D_0, D_1$ , and  $D_2$ .  $D_0$  is also known as a capacity dimension; it is independent of  $q$  and provides global (or average) information on the system (Voss 1988).  $D_1$  is related to the information or Shannon entropy (Shannon and Weaver 1949), and quantifies the degree of disorder present in a distribution. According to Gouyet (1996), for a measure  $\mu \in (0, 1)$ , the value of  $D_1$  is in the range of  $0 < D_1 < 1$ . A  $D_1$ ; a value close to 1.0 characterizes a system uniformly distributed throughout all scales, whereas a  $D_1$  close to 0 reflects a subset of the scale in which the irregularities are concentrated.  $D_2$  is mathematically associated with the correlation function (Grassberger and Procaccia 1983) and computes the correlation of measures contained in intervals of size  $\varepsilon$ . The relationship between  $D_0, D_1$ , and  $D_2$  is  $D_2 \leq D_1 \leq D_0$ , where the equality  $D_0 = D_1 = D_2$  occurs only if the fractal is statistically or exactly self-similar and homogeneous (i.e., monofractal) (Korvin 1992).

### 25.3 Multifractal Characterization of PSD in Fresh and Frozen-Thawed Apple Tissue

An apple fruit is mainly composed of the fleshy tissue of parenchyma cells permeated with vascular and intercellular air spaces (Esau 1977). The structural geometry of these intercellular spaces, or porous media, plays a fundamental role in governing the fluid and gas transport through its tissue (Celia et al. 1995; Dražeta et al. 2004). In general, the gas-filled intercellular spaces in plant organs are considered as the predominant pathways for gas transport through the plant and are greatly related to the characteristics of gas exchange (Raven 1996; Kuroki et al. 2004). The volume of air increases during fruit growth and occupies a considerable proportion of the fruit at harvest (Harker and Ferguson 1988; Yamaki and Ino 1992). This increase in air space is accompanied by a proportional decline in fruit density, while the density of the fruit cells themselves remains roughly constant (Westwood et al. 1967; Baoping 1999). In addition, the microstructure and fraction of intercellular air differs between cultivars and also between positions in the parenchyma tissue of the same fruit (Baumann and Henze 1983; Vincent 1989). Larger fruits of the same cultivar have a higher proportion of air than smaller fruits (Volz et al. 2004). Therefore, the characterization of these intercellular air spaces and distribution based on microstructural properties and realistic percolation models have important agricultural applications, since they are related to the understanding of fruit physiology and postharvest quality of the fruit during preservation. Fruits with greater fractional air volumes have been shown to be softer (Yearsley et al. 1997a, b; Volz et al. 2004), or more mealy (Harker and Hallet 1992), and to have greater internal gas diffusion rates (Rajapakse et al. 1990; Ho et al. 2006). Furthermore, the volume of these intercellular air spaces continues to increase during storage, and therefore, its measurement can be used to define the age of the fruit and also to characterize the effects of different storage conditions on its quality (Khan and Vincent 1990; Harker et al. 1999). All these features could be related to its known susceptibility to internal tissue browning and breakdown (Cheng et al. 1998).

On the other hand, freezing is a well-known preservation method widely used in the food industry. It involves lowering the product temperature generally to  $-18^{\circ}\text{C}$  or below. At temperatures lower than  $-10^{\circ}\text{C}$ , few microorganisms can develop, chemical reactions rates are greatly reduced, and cellular metabolic reactions are also delayed (Delgado and Sun 2001). One of the key issues in maintaining the shelf-life and other quality attributes of frozen food is ice crystallization (Kennedy 2003). The freezing process combines the favorable effect of low temperatures with the conversion of water into ice. The water–ice transition has the advantage of fixing the tissue structure and separating the water fraction in the form of ice crystals in such a way that water is not available either as a solvent or a reactive component (Delgado and Sun 2001). However, the size and location of the ice crystals may damage cell membranes and break down the physical structure. Thus, the cause of the undesirable physico-chemical modifications during freezing

is the crystallization of water and sometimes solutes (Martino et al. 1998; Delgado and Sun 2001). Slow freezing generally leads to large ice crystals formed exclusively on extracellular areas, which can damage cell structure and affect the thaw behavior as well as have an effect on the sensory properties and nutritional value of foodstuffs, while high freezing rates produce small crystals evenly distributed all over the tissue. Therefore, extended research has been carried out to control the crystal size. Conventional cooling methods, such as air blast, plate contact, circulating brine, and liquid nitrogen (ordered in increasing values of the heat transfer coefficient) are the most common methods used for food freezing (Sun 2001). Among these traditional methods, the immersion freezing process offers numerous advantages, e.g., high-heat-transfer coefficients, individualized freezing, good product quality, energy savings, etc.

We believe that the spectrum of local fractal dimensions could be an indication of geometric characteristics of PSD in fresh and frozen-thawed apples. This hope is solidly based on the fact that the fractal approach provides multifractal outputs that can be adjusted in order to fit multifractal spectra obtained from experimental data. Furthermore, it is well known that deviation from local fractal dimensions is greater for nonuniforms or natural plant structures such as pore distribution in apples; therefore, local fractal dimensions measured within a small region may vary from point to point, and the object can be characterized by a spectrum of fractal dimensions. Multifractal analysis (MFA) may improve characterization and discrimination of changes with high precision in apple tissue microstructure due to processing and preservation.

### 25.3.1 *Experimental Procedure for Apple Tissue*

Figure 25.1 illustrates the experimental procedure for apple sampling, the reconstructed X-ray image acquisition projection, and the stack of cropped X-ray images used for further processing and MFA. In this example, a Granny Smith apple (*Malus domestica*) with ~8.5 cm dia. (86.9% w/w moisture and ~12°Brix) was selected from a local market in Dublin (Ireland) and stored at  $4 \pm 1^\circ\text{C}$  for use later that same day. This apple variety was chosen as a test material due to the uniformity of its tissues and its structural stability in storage (Sterling 1968). In addition, the Granny Smith variety was available all over Ireland that year at a fairly constant quality. In spite of this, it is well known that high microstructural variability exists among apples even coming from the same lot, and therefore for analysis, the samples were extracted from the same apple. The apple cylinders (i.e., two fresh and two frozen samples) measuring 1.8 cm dia. and 2.5 cm high were cut using a cork borer in radial orientation from the middle parenchyma (~10 mm from the skin; Fig. 25.1a) and the same spatial position around the fruit. What remained of the fruit tissue was used for initial water content and soluble solids determination.

Frozen samples were obtained by immersing samples in a bath system filled with a freezing solution of 50% ethylene glycol and 50% water in volume. All samples

(fresh and frozen) were loosely wrapped in tissue paper saturated with water to prevent browning reactions, and kept together in a refrigerator for  $24 \text{ h}$  at  $4 \pm 1^\circ\text{C}$  to achieve uniform initial temperature and thawing of the frozen samples, and until apple cylinders were imaged. Moisture loss or water uptake during this period was considered to have little effect.

Samples were scanned with an X-ray micro-CT scanner (SCANCO MEDICAL AG,  $\mu\text{CT-40}$ , Bassersdorf, Switzerland) over the interval  $0^\circ\text{--}180^\circ$  (using a  $0.9^\circ$  scan step) at a linear resolution of  $10 \mu\text{m}$  by pixel, operating voltage of  $70 \text{ kV}$ , current of  $114 \mu\text{A}$ , and exposure time of  $8.4 \text{ s}$ . To account for the nonuniformities in the X-ray beam and nonuniform response of the CCD detector, the raw images were corrected for dark and white fields by averaging the flat field correction references collected at the beginning of the experiment. Each sample was enclosed in a plastic tube to avoid dehydration without any special preparation. The imaging process took approximately  $25 \text{ min}$  per sample.

The X-ray shadow projections of the 3-D object, digitalized as  $2,048 \times 2,048$  pixels, were processed using a mathematical back-projection procedure to obtain reconstructed cross-section images of linear attenuation coefficient values with 256 gradations (8-bit) (Fig. 25.1b). Thus, a stack of 200 cross-sections of grey images of the object (considering apple tissue and image background), with a  $10 \mu\text{m}$  interslice distance, was obtained from each scanned apple sample. Thus, for each set of radiographic images, to extract only the apple tissue image, a fixed area in the midsection of the scanned region ( $1,024 \times 1,024$  pixels, equivalent to  $104.9 \text{ cm}^2$ ) was cropped and then subjected to image analysis (Fig. 25.1c).

To obtain binary images for the consecutive MFA, the pores need to be identified and segmented at a certain threshold. However, the distinctions among the voids and solid phases in the radiographic images of apple tissue are frequently not sharp. They do not show a bimodal distribution due to the amount of peak overlap in the attenuation coefficient histogram (Mendoza et al. 2007); as a result, dedicated segmentation algorithms need to be used to closely represent the pore structure in the images. Therefore, partition of apple tissue images into pores and cellular

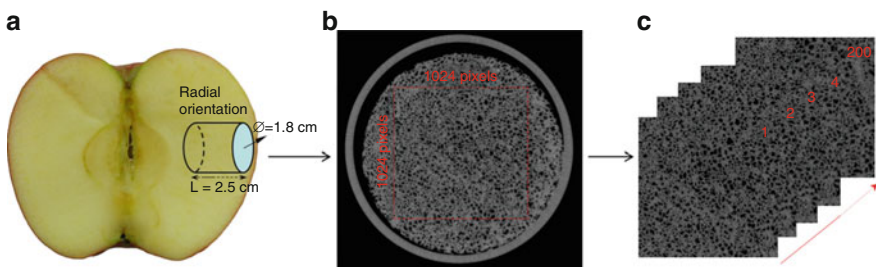


**Fig. 25.1** Illustration of experimental procedure for MFA of a fresh apple sample: (a) Sampling in radial orientation; (b) representative X-ray cross-sectional image reconstructed with 256 gradations, showing the *cropped region* ( $1,024 \times 1,024$  pixels<sup>2</sup>; *black regions* represent pores; *gray regions* represent cellular material); (c) stack of cropped radiographic images used for further processing and MFA

material was performed using the kriging-based segmentation algorithm developed by Oh and Lindquist (1999). The algorithm is a nonparametric formulation able to analyze regions of uncertainty based on the estimation of spatial covariance of the image in conjunction with the indicator kriging to determine object edges (Mardia and Hainsworth 1988). More details about the scanning process and segmentation algorithm of radiographic apple tissue images can be found in Mendoza et al. (2007).

### 25.3.2 *Extracted Features and Multifractal Spectrum Computation*

The fractal properties were extracted from digitized binary images of fat-connective tissue structures; 200 images from each type of apple sample, fresh or frozen-thawed, were evaluated. Parameters calculated from each multifractal spectrum were: the *Hausdorff dimension*,  $f(\alpha)$ ; the *singularities of strength*,  $\alpha$ ; and their *generalized fractal dimension*,  $D_q$ ; all were calculated in the range of moment orders ( $q$ ) between  $-10$  and  $+10$  taken at  $0.1$  lag increments. In addition, the bulk porosity of each apple sample, representing the void space as a fraction of the total volume, was calculated from the binary segmented images by a simple count of the pixels in the pore space divided by the total number of pixels in the image. Since the X-ray CT technique gave a stack of 200 images per sample, the average value of the computed multifractal parameters and spectrums from each stack of images and repetition were reported and used in further analyses.

To calculate the  $f(\alpha)$ -spectra, the method developed by Chhabra and Jensen (1989) was implemented in Matlab v7.0 (MathWorks, Inc., USA). Figure 25.2 illustrates the multifractal theory applied to a binary image of fresh apple tissue corresponding to the cropped image shown in Fig. 25.1b. Thus, images were partitioned using the box-counting algorithm to estimate the probability of containing pores (voids) for each box size  $\varepsilon$ , from 2 to 1,024 (i.e., in steps of  $2^k$ ,  $1 < k < 10$ ). From this information the partition functions and mass or correlation exponent of the  $q$ th order  $\tau(q)$  were obtained, as shown in Fig. 25.2b, c. Doing this for images that are  $1,024 \times 1,024$  pixels avoids artifacts, which occur when boxes do not entirely cover the image at the borders. A family of normalized measures,  $\mu_i(q, \varepsilon)$ , was constructed for positive and negative values of  $q$  covering variable ranges in steps of  $0.1$ :

$$\mu_i(q, \varepsilon) = \frac{P_i^q(\varepsilon)}{\sum_{i=1}^{N(\varepsilon)} P_i^q(\varepsilon)} \quad (25.12)$$

where  $P_i(\varepsilon)$  is the fraction (or probability) of pores contained in each  $i$ th box size  $\varepsilon$ . Note that for any value of  $q$ , the normalized measures take values in the interval  $(0, 1)$ . The direct computation of  $f(\alpha)$  values was made using the simplified relations proposed by Chhabra et al. (1989), and Chhabra and Jensen (1989):



$$f(q) = \lim_{\varepsilon \rightarrow 0} \frac{\sum_{i=1}^{N(\varepsilon)} \mu_i(q, \varepsilon) \cdot \log[\mu_i(q, \varepsilon)]}{\log \varepsilon} \tag{25.13}$$

Similarly, values of  $\alpha(q)$  were computed by evaluating:

$$\alpha(q) = \lim_{\varepsilon \rightarrow 0} \frac{\sum_{i=1}^{N(\varepsilon)} \mu_i(q, \varepsilon) \cdot \log[P_i(\varepsilon)]}{\log \varepsilon} \tag{25.14}$$

For each  $q$ , values  $f(q)$  and  $\alpha(q)$  were obtained from the slope of plots of the numerators in (25.13) and (25.14) versus  $\log \varepsilon$  over the entire range of  $\varepsilon$  values considered. The range of  $q$  values over which both functions were linear ( $\Delta q$ ) was selected considering the coefficients of determination ( $R^2$ ) of both fits (Fig. 25.2d, e). The  $f(q)$  and  $\alpha(q)$  functions (Fig. 25.2f) obtained over a given  $\Delta q$  were used to construct  $f(\alpha)$ -spectra as an implicit function of  $q$  and  $\varepsilon$ . The symmetry of multifractal spectra was evaluated by comparing the width of the spectra from their center [ $\alpha(0)$ ] to  $\alpha(|q_i|)$ . Values of  $|q_i|$  were the same in both the positive and negative domains and equal to the smaller of the two defining the  $\Delta q$  interval.

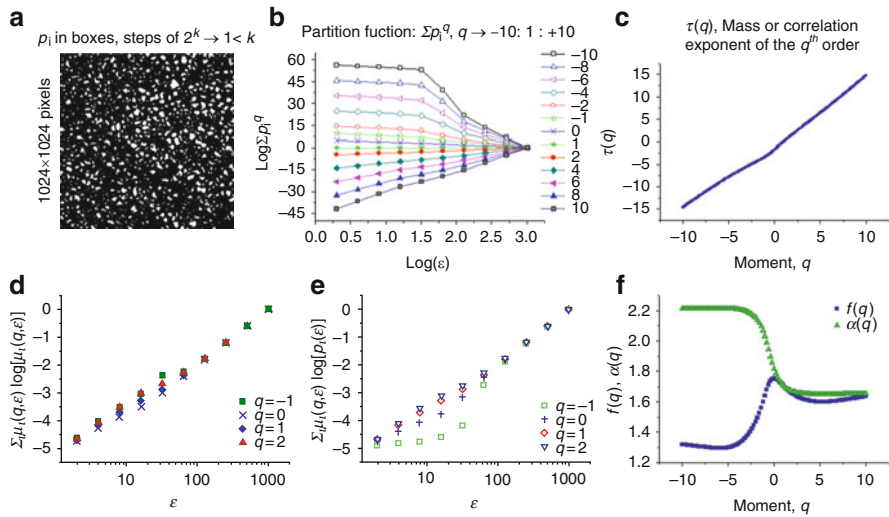


**Fig. 25.2** Illustration of multifractal theory applied to a binary image of fresh apple tissue (corresponding to *cropped image* in Fig. 25.1b): (a) Binary image (pores are represented by *white pixels*); (b) partition functions calculated in range of moment orders ( $q$ ) between  $-10$  and  $+10$ , but showing only lag increments of  $2$ ; (c) mass or correlation exponent of the  $q$ th order  $\tau(q)$ ; (d) and (e) Plots of (25.14) and (25.13), respectively, as a function of  $\varepsilon$ ; (f) Illustration of  $f(q)$  and  $\alpha(q)$  spectrums

On the other hand, generalized dimensions were obtained as the slope of the partition function over box size, both taken as logarithms (25.8) and (25.9). This method is known as the method of moments (Everstz and Mandelbrot 1992) or Rényi spectrum (Rényi 1995), as  $D_q$  is estimated for every moment  $q$ .

### 25.3.3 Results of MFA for PSD in Apples

To give a better idea about the microstructure of apple tissue, Fig. 25.3 shows representative radiographic images extracted from fresh and frozen-thawed apple tissue. The samples are characterized by different porous structures, illustrating the deleterious effect of freezing on the apple's microstructure. In the frozen-thawed sample, the cell disruption and tissue due to ice crystal formation is evident, wherein the pores are larger and rounded compared to fresh apple tissue. Also, differences (heterogeneity) in the bulk porosity distribution between cultivars are visually evident (Table 25.1). The average porosity computed from two stacks of apple images extracted from the same fruit (taken parallel to the medial axis of each fruit,  $0^\circ$  and  $180^\circ$  around the fruit; 200 images per stack, area per image =  $104.9 \text{ cm}^2$ ) showed values  $14.1 \pm 0.8\%$  for fresh and  $20.7 \pm 1.4\%$  for frozen-thawed tissue. ANOVA analysis of the average porosity confirmed the differences ( $P$ -value  $< 0.05$ ) between apple samples and revealed a higher variability between images from frozen-thawed tissue than those computed from fresh tissue, as represented by their standard deviations.

A crucial step in MFA is to determine the range of both  $\varepsilon$  and the moments of order  $q$  over which a multifractal method is applicable. This means determining the range of  $\varepsilon$  and  $q$  in which the numerators of (25.13) and (25.14) are linear functions of  $\log \varepsilon$ . The range of  $q$  values was selected considering the coefficients of determination ( $R^2$ ) of the fits (Fig. 25.2d, e). In this study, the general criterion was to choose the range of moments with  $R^2$  equal or larger than 0.95. Thus, the condition was met for  $\alpha(q)$  in the range  $\Delta q$  of  $-10$  to  $+10$ , and for  $f(q)$  in the range  $\Delta q$  of  $-1.4$  to  $+5.8$ , for both fresh and frozen-thawed samples.

The corresponding  $f(\alpha)$ -spectra and Rényi spectra (range of moment order  $q$  between  $-10$  and  $+10$ ) for each apple type are shown in Fig. 25.4a, b, respectively. The  $f(\alpha)$ -spectra shows the typical hump-shape observed for multifractal objects, but there are distinct differences in shape and symmetry between the fresh and frozen-thawed apple samples (Fig. 25.4a). The curvature and symmetry

**Table 25.1** Selected multifractal parameters and standard deviations from the analysis of binary images of pores for fresh and frozen-thawed apple tissue

	Porosity (%)	$\alpha(0) - \alpha(1)$	$\alpha(-1) - \alpha(0)$	$D_0 - D_1$	$f[\alpha(-1)] - D_0$	$D_1/D_0$
Fresh	$14.1 \pm 0.8^x$	$0.214 \pm 0.015^x$	$0.602 \pm 0.084^x$	$0.090 \pm 0.006^x$	$0.190 \pm 0.015^x$	$0.955 \pm 0.003^x$
Frozen	$20.7 \pm 1.4^y$	$0.229 \pm 0.016^y$	$0.791 \pm 0.129^y$	$0.092 \pm 0.008^y$	$0.238 \pm 0.025^y$	$0.954 \pm 0.003^y$

$x$ - $y$ , values with different letters within each column indicate significant differences among fresh and frozen apples ( $p < 0.05$ )

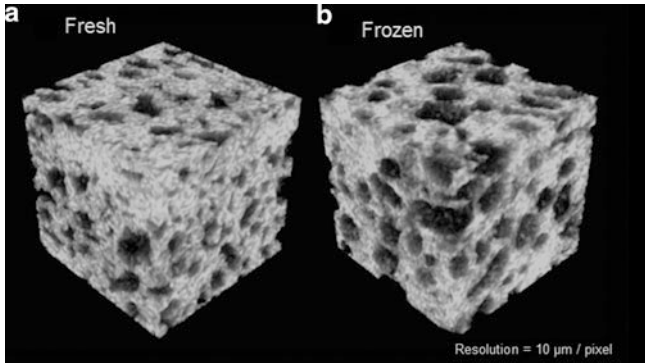


**Fig. 25.3** Reconstructed 3-D X-ray apple tissue images ( $200^3$  pixels $^3 \approx 8$  mm $^3$ ): (a) Fresh; (b) frozen-thawed tissue (*dark regions* represent pores; *clear regions* represent cellular material). The pore space in frozen-thawed tissue appears larger and apparently more heterogeneous in size than in fresh apple tissue, evidencing the deleterious effect of freezing on the apple microstructure

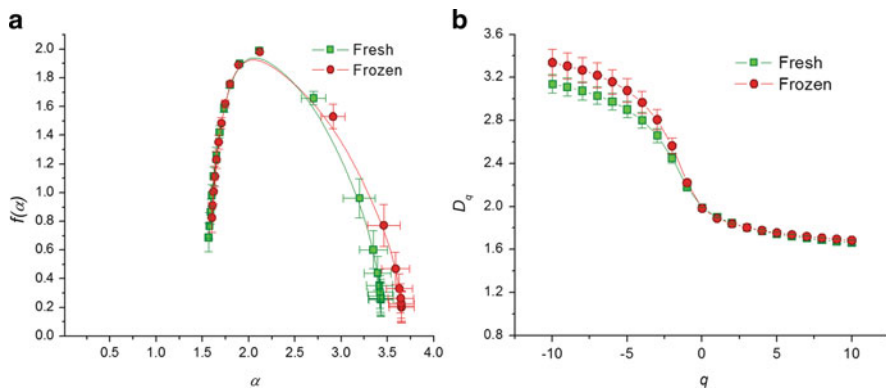


**Fig. 25.4** Multifractal spectrums of PSD in fresh and frozen-thawed apple tissues expressed by: (a)  $f(\alpha)$ -spectra; (b) Rényi dimensions spectra,  $D_q$

of the  $f(\alpha)$ -spectra provide information on the heterogeneity of a system, defined by the diversity of scaling exponents needed to characterize it. A homogeneous fractal exhibits a narrow  $f(\alpha)$ -spectra, whereas the opposite is true for a heterogeneous fractal. Thus, PSD in fresh apple tissue is more homogeneous than in frozen-thawed tissue as revealed by their  $f(\alpha)$ -spectra in Fig. 25.4a.

On the other hand, the Rényi spectra or generalized dimensions of the long transect are sigma-shaped curves with a clear asymmetry with respect to the cut point and the vertical axis; there is much more curvature for negative values of  $q$  than for positive values, which tend to be constant (Fig. 25.4b). More specifically, they exhibited pronounced decreasing  $D_q$  values with increasing  $q$ , and showed clear statistical differences between apple samples for  $D_q$  values with moments lower than  $q = 0$ . In this example, the evaluated range of  $D_q$  ran from  $D_{-10} = 3.140 \pm 0.086$

to  $D_{+10} = 1.664 \pm 0.022$  for fresh apple tissue, and from  $D_{-10} = 3.339 \pm 0.122$  to  $D_{+10} = 1.686 \pm 0.021$  for frozen-thawed tissue. However, the width of the  $D_q$ -spectra was greater in the frozen-thawed tissue, which indicated that the heterogeneity of PSDs in the parenchyma tissue was more apparent than in fresh apple, also confirming that the visual differences appreciated in the reconstructed 3-D images in Fig. 25.3.

In addition, heterogeneity can be assessed at  $q = 0$  by the magnitude of differences in the values  $D_0$  and  $\alpha(0)$ , or more generally, by the magnitude of changes around  $D_0$  in both  $f(\alpha)$  and  $\alpha$  axes. Table 25.1 shows selected multifractal parameters for characterizing the heterogeneity of fresh and frozen-thawed apple samples. In the present example, except for  $D_1/D_0$ , the computed parameters ( $\alpha(0) - \alpha(1)$ ,  $\alpha(-1) - \alpha(0)$ ,  $D_0 - D_1$ , and  $f[\alpha(-1)] - D_0$ ) showed statistical differences ( $P$ -value  $< 0.05$ ) between apple samples. In a symmetric spectrum, the widths ranging from  $\alpha(0)$  to  $\alpha(|q_i|)$ , and  $D_0$  to  $D_{(|q_i|)}$  are expected to be similar and smaller. In this sense, the results presented in Table 25.1 clearly confirm that PSD in fresh apple tissue is more homogeneous than that of frozen-thawed tissue. This tendency toward homogeneity implies that regions with high and low concentration of mass (pores) scale similarly.

## 25.4 Multifractal Characterization of FSD for Two Qualities of Presliced Pork Hams

In ham products, FSD is a fundamental physical property analyzed in assessing product quality. Here, FSD is related to sensory properties such as texture, taste, quality of the raw meat, and visual appearance. Therefore, accurate representation of this microstructural property is needed for an objective quality characterization and prediction during ham formulation. Moreover, ham slices in general have complex and inhomogeneous colored surfaces, and textures do not contain any detectable periodic or quasiperiodic structure. Instead, textures exhibit random but persistent patterns that result in a cloud-like appearance (Mendoza et al. 2009). These inhomogeneities can be attributed mainly to formulation, presence of pores/defects and fat-connective tissue, and color variations (Valous et al. 2009). Thus, for objective characterization, image analysis techniques need to take into account the high variability in texture appearance. Consequently, fractal metrics and concepts have been recently applied to investigate and describe the complexities and self-similarities of a variety of ham surfaces (Mendoza et al. 2009; Valous et al. 2009).

Similar to the multifractal characterization of PSD in fresh and frozen-thawed apple tissues (10  $\mu\text{m}/\text{pixel}$ ), we have presented an application of multifractal theory for characterization of FSD in two qualities of presliced pork hams typically consumed in Ireland. Here, the extracted multifractal parameters and spectrums were computed using the same principles and conditions mentioned above; nevertheless, it is important to note that the MFA in this case was tested for characterization of structures segmented from ham images captured at the macroscale level (0.102 mm/pixel).

### 25.4.1 Experimental Procedure for Ham Samples

Two qualities of pork hams were manufactured at Dawn Farm Foods Co. (Kildare, Ireland), using different muscle sections and various percentages of brine solutions (wet curing by injection). Specifically, the *high yield ham* (low quality) had a 50% brine injection and was made from pork muscle called Silverside PAD (biceps femoris), cut to 100 mm width. The injected muscle was vacuum-tumbled at 1,500 rpm for 12 h and vacuum-filled into PVC casings, clipped, and cooked at 82°C to a core temperature of 72°C. The *medium-yield ham* (intermediate quality) had a 30% brine injection and contained three leg muscles: Topside, Silverside, and Knuckle. The injected muscle was vacuum-tumbled at 500 rpm for 5 h and vacuum-filled into PVC casings, clipped, and cooked at 82°C to a core temperature of 72°C. All pork ham samples were chilled to 4°C before slicing. Images were acquired immediately after slicing (100 slices per type of ham quality).

To ensure reproducibility in the preprocessing and MFA of ham images, a color-calibrated computer vision system (CVS) as described by Valous et al. (2009) was used for image acquisition (spatial resolution 0.102 mm/pixel). Then, a polynomial transform was used for signal calibration of the captured images (Valous et al. 2009), which mapped the raw RGB primary signals into the sRGB color standard (IEC 1999). These color-calibrated images were used in the identification and segmentation of fat-connective tissue structures. For analysis, due to the large variation in size and shape between the two presliced ham qualities, the images were subsequently cropped in the central region to produce  $512 \times 512$  pixel images (equivalent to 2,727.4 mm<sup>2</sup>). The software package MATLAB (MathWorks, USA) was used for image processing and multifractal computations.

The fat-connective tissue segmentation was performed using the green (G) intensity images (from sRGB), since visually this color channel better represented the edges of the fat-connective tissue structures of the two evaluated hams. Thus, the green (G) intensity image was preprocessed with a median filter ( $3 \times 3$ ) to remove impulse noise. Then, a morphological closing filter ( $3 \times 3$ ) was applied to remove pores; a decrease in the intensity variations of the background pixels (more “flat” background in relation to fat-connective tissue) was also carried out. A hi-pass filter ( $15 \times 15$ ) was applied for increasing sharpness and contrast. This operation introduced some random noise, which was then removed using the median filtering operation ( $3 \times 3$ ), while a subsequent histogram-based segmentation using a unique threshold value of 200 produced the binary images (Valous et al. 2009).

Figure 25.5 shows representative images of the two evaluated pork ham qualities as well as the experimental procedure for cropping and binarization of the fat-connective tissue structures. The original ham images were cropped to obtain three square regions ( $512 \times 512$  pixels<sup>2</sup>) from each slice; since not all ham slices had the same spatial dimensions, this process allowed receiving representative information from each quality sample, facilitating better scrutiny and interpretation, and also keeping computation times manageable. Also, the depicted binary images confirm the performance of the segmentation method used in this investigation.

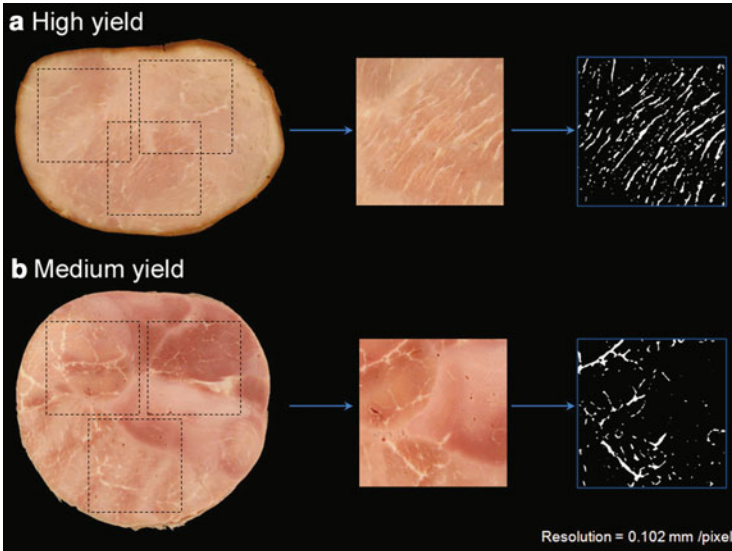


**Fig. 25.5** Illustration of experimental procedure for MFA using ham samples: (a) Representative images of the two evaluated pork ham qualities; (b) cropped color regions ( $512 \times 512$  pixels<sup>2</sup>); (c) corresponding binary images of segmented fat-connective tissue structures used for further processing and MFA

### 25.4.2 Results of MFA for FSD in Hams

As observed in Fig. 25.5, the evaluated ham qualities are characterized by different contents and distributions of fat-connective tissue structures; they also show a high variability in the textural appearance of slices from the same quality type. Fat-connective tissue estimations (average of 300 square images per quality type) showed values for high yield of  $6.2 \pm 2.1\%$  and for medium yield  $2.9 \pm 1.6\%$ . The statistical differences ( $P$ -value  $< 0.05$ ) were evident between these average indices (Table 25.2).

The range of  $q$  values for ham samples, considering the coefficients of determination ( $R^2$ ) equal or larger than 0.95, for the plot of numerators (25.13) and (25.14) versus  $\log \varepsilon$ , were for  $\alpha(q)$  in the range  $\Delta q$  of  $-1.7$  to  $+10$  and for  $f(q)$  in the range  $\Delta q$  of  $-1.6$  to  $+3.1$  for both ham qualities.

Figures 25.6a, b depict the average  $f(\alpha)$ -spectra and Rényi spectra for each ham quality and their standard deviations for each point, respectively. The  $f(\alpha)$ -spectra revealed that FSD in medium-yield hams is slightly more homogeneous than in high-yield hams (Fig. 25.6a), as indicated by the shorter amplitude and symmetric shape of the average  $f(\alpha)$ -spectra for the medium-yield ham. Similarly, the Rényi spectra (Fig. 25.6b) exhibited pronounced decreased  $D_q$  values with increasing  $q$ , and showed clear statistical differences between the ham qualities in the entire range of  $D_q$  values (with  $q$  moments ranging from  $-10$  to  $+10$ ). In this example, the

**Table 25.2** Selected multifractal parameters and standard deviations from the analysis of binary images of fat-connective tissue for the two qualities of presliced hams

	Fat-connective tissue index (%)	$\alpha(0) - \alpha(1)$	$\alpha(-1) - \alpha(0)$	$D_0 - D_1$	$f[\alpha(-1)] - D_0$	$D_1/D_0$
High	$6.23 \pm 2.07^x$	$0.385 \pm 0.042^x$	$0.616 \pm 0.069^x$	$0.164 \pm 0.020^x$	$0.267 \pm 0.023^x$	$0.909 \pm 0.013^x$
Medium	$2.89 \pm 1.56^y$	$0.393 \pm 0.070^y$	$0.470 \pm 0.119^y$	$0.174 \pm 0.029^y$	$0.233 \pm 0.054^y$	$0.888 \pm 0.021^y$

*x*-*y*, values with different letters within each column indicate significant differences among ham qualities ( $p < 0.05$ )

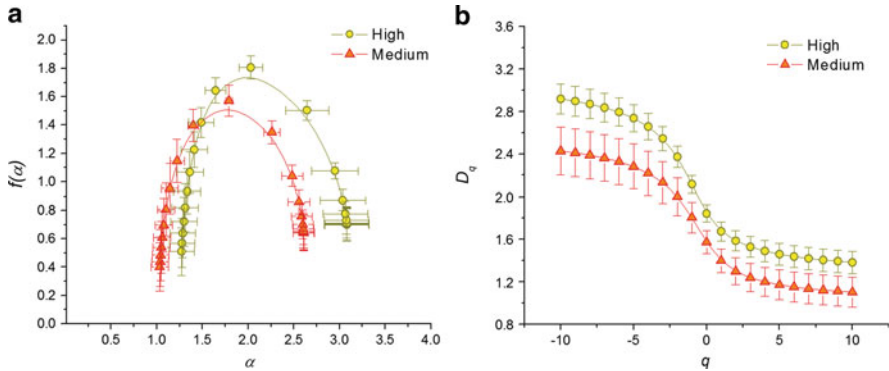


**Fig. 25.6** Multifractal spectra of FSD in two qualities of presliced hams expressed as: (a)  $f(\alpha)$ -spectra; (b) Rényi dimensions spectra,  $D_q$

evaluated range of  $D_q$  ran from  $D_{-10} = 2.920 \pm 0.142$  to  $D_{+10} = 1.382 \pm 0.107$  for high-yield hams and  $D_{-10} = 2.429 \pm 0.226$  to  $D_{+10} = 1.326 \pm 0.140$  for medium-yield hams, with an average  $D_0$  dimension for high- and medium-yield hams of  $1.808 \pm 0.080$  and  $1.572 \pm 0.180$ , respectively. Nonetheless, the width of  $D_q$ -spectra is greater in high-yield hams, which indicates that the heterogeneity of FSDs in the ham matrix is more apparent than in medium-yield types. In general, both multifractal spectrums allowed for a robust characterization of these two types of ham. The selected multifractal parameters presented in Table 25.2 confirm that, with exception of the difference  $\alpha(0) - \alpha(1)$  and in spite of the high variability of samples coming from the same quality, the computed parameters  $\alpha(-1) - \alpha(0)$ ,  $D_0 - D_1$ ,  $f[\alpha(-1)] - D_0$ , and  $D_1/D_0$  are all statistically different ( $P$ -value  $< 0.05$ ) and therefore could be used as quality predictors of hams.

## 25.5 Conclusions and Outlook

In this chapter, multifractal spectrum and the generalized dimensions of apple pore structure are computed with data obtained from X-ray images (10  $\mu\text{m}/\text{pixel}$ ) of fresh and frozen-thawed apple samples (Granny Smith), as well as color images (0.102 mm/pixel) of two different qualities of presliced pork hams typically

consumed in Ireland. The extracted multiscaling properties from binary images (of pores or fat-connective tissue structures) allowed evaluating and revealing the significance of the method in discrimination of morphology and distribution of pores and fat-connective tissue structures in these particular samples.

Multifractal parameters were found to reflect the major aspects of variability in the PSD of apple tissue and FSD of ham fat-connective tissue, providing a unique quantitative characterization of the spatial distribution data. The irregularity and complexity of apple pore structure and ham fat-connective tissue, together with its scale-invariant features suggest that multifractal distribution is a suitable and natural model.

The results of both examples have also demonstrated that MFA has significant benefits for quantitative analysis of the complex microstructure of biological materials from images, allowing conclusions to be drawn on the exact topography of, for example, PSD and FSD of apple tissue and presliced cooked pork hams. Potential multifractal parameters for characterizing contrasting PSD and FSD are  $D_0$ ,  $D_1$ ,  $\alpha(0) - \alpha(1)$ ,  $\alpha(-1) - \alpha(0)$ ,  $D_0 - D_1$ ,  $f[\alpha(-1)] - D_0$ , and  $D_1/D_0$ . Furthermore, modeling apple and ham images with multifractal spectrums, such as  $f(\alpha)$ -spectra and  $D_q$ -spectra, allows the capture of differentiating microstructural features and makes possible the automatic characterization, not only between apple varieties and ham types, but also between roughness degrees or image textures, due to the capability of the multifractal parameters to resolve local densities from images. Multifractal parameters are promising descriptors for type identification and quality assessment of apple and ham samples. Moreover, this multiscaling procedure and image analysis technique should provide valuable opportunities for further research of other natural and processed foods.

**Acknowledgements** The authors gratefully acknowledge the Food Institutional Research Measure (FIRM) strategic research initiative, as administered by the Irish Department of Agriculture and Food, for their financial support.

## References

- Baoping J (1999) Nondestructive technology for fruits grading. In: Proceedings of 1999 international conference on agricultural engineering, Beijing, China, pp IV127–IV133
- Baumann H, Henze J (1983) Intercellular space volume of fruit. *Acta Hort* 138:107–111
- Callen HB (1985) Thermodynamics and an introduction to thermostatistics, 2nd edn. Wiley, New York
- Celia M, Reeves P, Ferrand L (1995) Recent advances in pore scale models for multiphase flow in porous media. *Rev Geophys Suppl* 33:1049–1057
- Cheng Q, Banks NH, Nicholson SE, Kingsley AM, Mackay BR (1998) Effects of temperature on gas exchange of “Braeburn” apples. *NZ J Crop Hort Sci* 26:299–306
- Chhabra A, Jensen RV (1989) Direct determination of the  $f(\alpha)$  singularity spectrum. *Phys Rev Lett* 62(12):1327–1330
- Chhabra AB, Meneveu C, Jensen RV, Sreenivasan KR (1989) Direct determination of the  $f(\alpha)$  singularity spectrum and its application to fully developed turbulence. *Phys Rev A* 40:5284–5294



- Cox LB, Wang JSY (1993) Fractal surfaces: measurements and applications in earth sciences. *Fractals* 1:87–117
- Delgado AE, Sun D-W (2001) Heat and mass transfer models for predicting freezing process – a review. *J Food Eng* 47(3):157–174
- Dražeta L, Lang A, Alistair JH, Richard KV, Paula EJ (2004) Air volume measurement of “Braeburn” apple fruit. *J Exp Bot* 55:1061–1069
- Eghball B, Schepers JS, Negahban M, Schlemmer MR (2003) Spatial and temporal variability of soil nitrate and corn yield: multifractal analysis. *Agron J* 95:339–346
- Esau K (1977) *Anatomy of seed plants*. Wiley, New York
- Everstz CJG, Mandelbrot BB (1992) Multifractal measures. In: Peitgen H, Jürgens H, Saupe D (eds) *Chaos and fractals*. Springer, Berlin, pp 922–953
- Gouyet J-F (1996) *Physics and fractal structures*. Springer, New York
- Grassberger P, Procaccia I (1983) Characterization of strange attractors. *Phys Rev Lett* 50(5):346–349
- Halsey TC, Jensen MH, Kadanoff LP, Procaccia I, Shraiman BI (1986) Fractal measures and their singularities: the characterization of strange sets. *Phys Rev A* 33(2):1141–1151
- Harker FR, Ferguson IB (1988) Calcium ion transport across discs of the cortical flesh of apple fruit in relation to fruit development. *Physiol Plant* 74:695–700
- Harker FR, Hallet IC (1992) Physiological changes associated with development of mealiness of apple fruit during cool storage. *HortScience* 27:1291–1294
- Harker FR, Watkins CB, Brookfield PL, Miller MJ, Reid S, Jackson PJ, Bielecki RL, Bartley T (1999) Maturity and regional influences on watercore development and its postharvest disappearance in “Fuji” apples. *J Am Soc Hortic Sci* 124:166–172
- Hentchel HGE, Procaccia I (1983) The infinite number of generalized dimensions of fractals and strange attractors. *Physica D* 8:435–444
- Ho QT, Verlinden BE, Verboven P, Nicolai BM (2006) Gas diffusion properties at different positions in the pear. *Postharvest Biol Technol* 41:113–120
- IEC (1999) IEC 61966–2–1: multimedia systems and equipment – colour measurements and management – Part 2–1: colour management – default RGB color space – sRGB. International Electrotechnical Commission (IEC), Geneva, Switzerland
- Kennedy C (2003) Developments in freezing. In: Zeuthen P, Bøgh-Sørensen L (eds) *Food preservation techniques*. CRC Press, Cambridge/England, pp 228–240
- Ketipearachchi KW, Tatsumi J (2000) Local fractal dimensions and multifractal analysis of the root system of legumes. *Plant Prod Sci* 3:289–295
- Khan AA, Vincent JFV (1990) Anisotropy of apple parenchyma. *J Sci Food Agric* 52:455–466
- Korvin G (1992) *Fractals models in the earth sciences*. Elsevier, Amsterdam, The Netherlands
- Kravchenko AN, Boast CW, Bullock DG (1999) Multifractal analysis of soil variability. *Agron J* 91:1033–1041
- Kuroki S, Oshita S, Sotome I, Kawagoe Y, Seo Y (2004) Visualization of 3-D network of gas-filled intercellular spaces in cucumber fruit after harvest. *Postharvest Biol Technol* 33:255–262
- Mandelbrot BB (1992) *The fractal geometry of nature*, 2nd edn. W.H. Freeman, New York
- Mardia KV, Hainsworth TJ (1988) A spatial thresholding method for image segmentation. *IEEE Trans Pattern Anal Mach Intell* 6:919–927
- Martino MN, Otero L, Sanz PD, Zaritzky NE (1998) Size and location of ice crystals in pork frozen by high-pressure-assisted freezing as compared to classical methods. *Meat Sci* 50(3):303–313
- Mendoza F, Verboven P, Mebatsion HK, Kerckhofs G, Wevers M, Nicolai BM (2007) Three-dimensional pore space quantification of apple tissue using x-ray computed microtomography. *Planta* 226:559–570
- Mendoza F, Valous NA, Allen P, Kenny TA, Ward P, Sun D-W (2009) Analysis and classification of commercial ham slice images using directional fractal dimension features. *Meat Sci* 81(2):313–320
- Oh W, Lindquist W (1999) Image thresholding by indicator kriging. *IEEE Trans Pattern Anal Mach Intell* 21:590–602

- Pascual M, Ascioti FA, Caswell H (1995) Intermittency in the plankton: a multifractal analysis of zooplankton biomass variability. *J Plankton Res* 17:1209–1232
- Plotnick RE, Gardner RH, Hargrove WW, Prestegard K, Perlmutter M (1996) Lacunarity analysis: a general technique for the analysis of spatial patterns. *Phys Rev E* 53(5):5461–5468
- Rajapakse NC, Banks NH, Hewett EW, Cleland DJ (1990) Development of oxygen concentration gradients in flesh tissues of bulky plant organs. *J Am Soc Hortic Sci* 115:793–797
- Raven JA (1996) Into the voids: the distribution, function, development and maintenance of gas spaces in plants. *Ann Bot* 78:137–142
- Rényi A (1995) On a new axiomatic theory of probability. *Acta Mathematica Hungarica* VI 3–4:285–335
- Scheuring I, Riedi RH (1994) Application of multifractals to the analysis of vegetation pattern. *J Veg Sci* 5:489–496
- Shannon CE, Weaver W (1949) *The mathematical theory of communication*. University of Illinois Press, Chicago
- Sterling C (1968) Effect of low temperature on structure and firmness of apple tissue. *J Food Sci* 33:577–580
- Sun D-W (ed) (2001) *Advances in food refrigeration*. Leatherhead Publishing, LFRA Ltd, Surrey
- Valous NA, Mendoza F, Sun D-W, Allen P (2009) Colour calibration of a laboratory computer vision system for quality evaluation of pre-sliced hams. *Meat Sci* 81(1):132–141
- Vicsek T (1992) *Fractal growth phenomena*, 2nd edn. World Scientific Publishing, Singapore
- Vincent JFV (1989) Relationships between density and stiffness of apple flesh. *J Sci Food Agric* 31:267–276
- Volz RK, Harker FR, Hallet IC, Lang A (2004) Development of texture in apple fruit – a biophysical perspective. *Acta Hort* 636:473–479
- Voss RF (1988) Fractals in nature: from characterization to simulation. In: Peitgen H-O, Saupe D (eds) *The sciences of fractal images*. Springer, New York, pp 21–69
- Westwood MN, Batjer LP, Billingsley HD (1967) Cell size, cell number and fruit density of apples as related to fruit size, position in the cluster and thinning method. *Proc Am Soc Hort Sci* 91:51–62
- Xiaoyan G, Peiling Y, Shumei R, Yunkai L (2007) Multifractal analysis of soil structure under long-term wastewater irrigation based on digital image technology. *NZ J Agric Res* 50:789–796
- Yamaki S, Ino M (1992) Alteration of cellular compartmentation and membrane permeability to sugars in immature and mature apple fruit. *J Am Soc Hortic Sci* 117:951–954
- Yearsley CW, Banks NH, Ganesh S (1997a) Temperature effects on the internal lower oxygen limits of apple fruit. *Postharvest Biol Technol* 11:73–83
- Yearsley CW, Banks NH, Ganesh S (1997b) Effects of carbon dioxide on the internal lower oxygen limits of apple fruit. *Postharvest Biol Technol* 12:1–13